J. Fluid Mech. (2010), *vol.* 655, *pp.* 152–173.
doi:10.1017/S0022112010000820

Aspect ratio dependence of heat transfer and large-scale flow in turbulent convection

J. BAILON-CUBA, M. S. EMRAN† AND J. SCHUMACHER

Institut für Thermo- und Fluiddynamik, Technische Universität Ilmenau, Postfach 100565, D-98684 Ilmenau, Germany

(Received 7 January 2009; revised 8 February 2010; accepted 9 February 2010; first published online 12 May 2010)

The heat transport and corresponding changes in the large-scale circulation (LSC) in turbulent Rayleigh–Bénard convection are studied by means of three-dimensional direct numerical simulations as a function of the aspect ratio Γ of a closed cylindrical cell and the Rayleigh number Ra. The Prandtl number is $Pr = 0.7$ throughout the study. The aspect ratio Γ is varied between 0.5 and 12 for a Rayleigh number range between 10^7 and 10^9. The Nusselt number Nu is the dimensionless measure of the global turbulent heat transfer. For small and moderate aspect ratios, the global heat transfer law $Nu = A \times Ra^{\beta}$ shows a power law dependence of both fit coefficients A and β on the aspect ratio. A minimum of $Nu(\Gamma)$ is found at $\Gamma \approx 2.5$ and $\Gamma \approx 2.25$ for $Ra = 10^7$ and $Ra = 10^8$, respectively. This is the point where the LSC undergoes a transition from a single-roll to a double-roll pattern. With increasing aspect ratio, we detect complex multi-roll LSC configurations in the convection cell. For larger aspect ratios $\Gamma \gtrsim 8$, our data indicate that the heat transfer becomes independent of the aspect ratio of the cylindrical cell. The aspect ratio dependence of the turbulent heat transfer for small and moderate Γ is in line with a varying amount of energy contained in the LSC, as quantified by the Karhunen–Loève or proper orthogonal decomposition (POD) analysis of the turbulent convection field. The POD analysis is conducted here by the snapshot method for at least 100 independent realizations of the turbulent fields. The primary POD mode, which replicates the time-averaged LSC patterns, transports about 50 % of the global heat for $\Gamma \geqslant 1$. The snapshot analysis enables a systematic disentanglement of the contributions of POD modes to the global turbulent heat transfer. Although the smallest scale – the Kolmogorov scale η_K – and the largest scale – the cell height H – are widely separated in a turbulent flow field, the LSC patterns in fully turbulent fields exhibit strikingly similar texture to those in the weakly nonlinear regime right above the onset of convection. Pentagonal or hexagonal circulation cells are observed preferentially if the aspect ratio is sufficiently large ($\Gamma \gtrsim 8$).

1. Introduction

One of the most comprehensively studied turbulent flows is Rayleigh–Bénard convection, in which a complex three-dimensional turbulent motion is initiated by heating a fluid from below and cooling from above. Detailed measurements of the turbulent heat transport (e.g. Niemela *et al.* 2000; Amati *et al.* 2005; Funfschilling *et al.*

† Email address for correspondence: mohammad.emran@tu-ilmenau.de

2005; Ahlers, Grossmann & Lohse 2009), the statistics of temperature fluctuations and their gradients (Castaing *et al.* 1989; Emran & Schumacher 2008), and more recently, of coherent thermal plume structures (Zhou, Sun & Xia 2007; Shishkina & Wagner 2008), which carry the heat locally through the closed vessel, have been conducted. The variation of turbulent heat transfer with respect to two of the three dimensionless control parameters in thermal convection – the Rayleigh number Ra and the Prandtl number Pr – was the focus of most of the laboratory experiments and simulations. The dependence on the third control parameter, the aspect ratio $\Gamma = D/H$ with D being the sidelength or diameter and H the cell height, has been studied much less intensively.

Only a few systematic analyses of high-Rayleigh-number convection in flat cells with $\Gamma > 1$ have been reported (Fitzjarrald 1976; Wu & Libchaber 1992; Funfschilling *et al.* 2005; Hartlep, Tilgner & Busse 2005; Sun *et al.* 2005; Niemela & Sreenivasan 2006; du Puits, Resagk & Thess 2007) although the large aspect ratio setting is relevant for nearly all geophysical and astrophysical flows (e.g. Stein & Nordlund 2006) and many technological applications such as the energy-efficient design of indoor ventilation (e.g. Zerihun Desta *et al.* 2005). Furthermore, an explicit dependence on the aspect ratio is not contained in any of the existing scaling theories for the turbulent heat transfer (Siggia 1994; Grossmann & Lohse 2000). Grossmann & Lohse (2003) discussed geometry effects by including variations of the kinetic boundary layer thickness at the plates and sidewalls as a function of the aspect ratio. However, they found that the global heat transfer laws remained independent of Γ. This is because their argumentation is built on the volume flux conservation which requires a large-scale flow – a so-called 'wind of turbulence'. In fact all existing scaling theories require such a large-scale flow for the ansatz of their boundary layer dynamics. It is, however, well known that the coherent large-scale circulations (LSCs) present at $\Gamma \sim 1$ break down into more complex and less coherent patterns when the aspect ratio is increased far beyond unity. Such phenomena were reported by several authors: for example, by means of Fourier spectrum analysis (Hartlep, Tilgner & Busse 2003), plume structure visualizations (Shishkina & Wagner 2006) or comparisons of the autocorrelations of the temperature and velocity fields (du Puits *et al.* 2007).

In this work, we therefore want to study the dependence of convective turbulence on the aspect ratio in a cylindrical cell by three-dimensional direct numerical simulations (DNSs). Our focus is on aspect ratios Γ larger than unity. Values for Γ cover a range between 0.5 and 12 for Rayleigh numbers between 10^7 and 10^9. The Prandtl number is kept constant. The present analysis addresses the following three questions: Does the turbulent heat transfer at fixed Rayleigh and Prandtl numbers depend on the aspect ratio? Similar studies have been carried out by Fitzjarald (1976), Wu & Libchaber (1992), Funfschilling *et al.* (2005), Hartlep *et al.* (2005) and Sun *et al.* (2005). Which changes in the global flow structure are associated with an increase of the aspect ratio beyond unity? This aspect has been discussed in part in Hartlep *et al.* (2003) and du Puits *et al.* (2007). Which fraction of the total kinetic energy is carried and how much heat is transferred by the LSC? Answering the last question requires a systematic disentanglement of the turbulent large- and small-scale flow and temperature patterns. Therefore, we conduct proper orthogonal decomposition (POD) of the turbulent flow fields. We observe a dependence of the heat transfer – as measured by the dimensionless Nusselt number Nu – on Γ. This dependence is due to the rearrangement of the large-scale flow patterns with varying aspect ratio.

Although the flow is fully turbulent, the time-averaged velocity field patterns will exhibit morphological similarities with the structures which have been observed at the

onset of convection (Charlson & Sani 1971; Oresta, Stringano & Verzicco 2007) or in the weakly nonlinear regime right above the onset of convection (see e.g. Busse & Whitehead 1971; Clever & Busse 1989; Croquette 1989; Bodenschatz, Pesch & Ahlers 2000). For example, a transition from a one-roll to a two-roll flow pattern right above the critical Rayleigh number was found at an aspect ratio $\Gamma = 1.62$ in a cylindrical cell (Oresta *et al.* 2007). In a fully turbulent regime, such bifurcations are present at slightly larger aspect ratios. Furthermore, in the weakly nonlinear case, many specific configurations have been detected such as knot convection, spiral defect chaos and textures with wall foci (see Bodenschatz *et al.* 2000 for a review). We observe that the time-averaged flow fields for $Ra \geqslant 10^7$ yield similar patterns. Our findings will be in line with recent studies by Hartlep *et al.* (2005) in a rectangular cell with periodic sidewalls, in which emphasis was given to the variation of patterns with respect to the Prandtl number Pr at different aspect ratios. Large-scale flow patterns are also present in other closed turbulent flow systems, such as in high-Reynolds-number turbulence in von Kárman swirling flows (La Porta *et al.* 2001) or Taylor vortex flows (Lathrop, Fineberg & Swinney 1992).

The outline of the paper is as follows. In § 2, we summarize the numerical model and the equations of motion. Section 3 discusses the dependence of the Nusselt number on the aspect ratio for fixed Rayleigh numbers and the Nusselt number as a function of the Rayleigh number at fixed aspect ratio. Section 4 studies the LSC. Section 5 describes the POD analysis and the contributions of different POD modes to the heat transfer. We conclude with a summary and outlook in § 6.

2. Numerical model

The Navier–Stokes equations for an incompressible flow in the Boussinesq approximation are solved in combination with the advection–diffusion equation for the temperature field in cylindrical coordinates. The system is given by

$$\frac{\partial \boldsymbol{u}}{\partial t} + (\boldsymbol{u}\cdot\nabla)\boldsymbol{u} = -\nabla p + \nu\nabla^2\boldsymbol{u} + \alpha g T \boldsymbol{e}_z, \tag{2.1}$$

$$\nabla\cdot\boldsymbol{u} = 0, \tag{2.2}$$

$$\frac{\partial T}{\partial t} + (\boldsymbol{u}\cdot\nabla)T = \kappa\nabla^2 T, \tag{2.3}$$

where $p(\boldsymbol{x}, t)$ is the kinematic pressure, $\boldsymbol{u}(\boldsymbol{x}, t)$ the velocity field, $T(\boldsymbol{x}, t)$ the total temperature field, ν the kinematic viscosity and κ the diffusivity of the temperature. Our studies are conducted for $Pr = \nu/\kappa = 0.7$. The Rayleigh numbers $Ra = \alpha g \Delta T H^3/(\nu\kappa)$ span a range from 10^7 to 10^9. Here, α is the thermal expansion coefficient, g the gravitational acceleration and ΔT the outer temperature difference. The horizontal plates have no-slip boundary conditions, i.e. $\boldsymbol{u} \equiv 0$, at a fixed temperature. The side walls are adiabatic no-slip boundaries, i.e. $\boldsymbol{u} \equiv 0$ and $\partial T/\partial r = 0$. Small effects of finite conductivity – as present in the experiments – are thus excluded.

The equations are discretized on a staggered grid with a second-order finite difference scheme (Verzicco & Camussi 2003; Verzicco & Orlandi 1996). The pressure field p is determined by a two-dimensional Poisson solver after applying a one-dimensional fast Fourier transform (FFT) in the azimuthal direction. The time advancement is done by a third-order Runge–Kutta scheme. The grid spacings are non-equidistant in the radial and vertical directions. In the vertical direction, the grid spacing corresponds to the Tschebycheff collocation points. The grid resolutions employed in all runs are listed in table 1. The numerical effort grows with Γ^2 in the

$N_\phi \times N_r \times N_z$	Ra	Γ	t/t_f	$Nu \pm \sigma$	σ in %
$97 \times 65 \times 128$	10^7	0.50	300	17.08 ± 0.07	0.4
$193 \times 97 \times 128$	10^7	1.00	150	16.73 ± 0.08	0.5
$217 \times 133 \times 128$	10^7	1.50	111	16.37 ± 0.08	0.5
$217 \times 133 \times 128$	10^7	1.75	151	16.11 ± 0.03	0.2
$217 \times 133 \times 128$	10^7	2.00	250	15.88 ± 0.07	0.4
$217 \times 133 \times 128$	10^7	2.25	251	15.97 ± 0.04	0.2
$257 \times 165 \times 128$	10^7	2.50	251	15.77 ± 0.03	0.1
$257 \times 165 \times 128$	10^7	2.75	251	15.97 ± 0.04	0.3
$257 \times 165 \times 128$	10^7	3.00	150	16.06 ± 0.05	0.3
$301 \times 211 \times 128$	10^7	4.00	150	16.22 ± 0.03	0.2
$385 \times 281 \times 128$	10^7	6.00	150	16.66 ± 0.04	0.2
$401 \times 311 \times 128$	10^7	8.00	150	17.44 ± 0.02	0.1
$513 \times 361 \times 128$	10^7	10.00	150	17.34 ± 0.03	0.2
$601 \times 401 \times 128$	10^7	12.00	150	17.49 ± 0.03	0.2
$151 \times 81 \times 160$	5×10^7	0.50	150	26.20 ± 0.21	0.8
$257 \times 129 \times 160$	5×10^7	1.00	150	25.86 ± 0.13	0.5
$271 \times 151 \times 160$	5×10^7	2.00	149	25.83 ± 0.12	0.5
$401 \times 225 \times 160$	5×10^7	3.00	145	25.90 ± 0.05	0.2
$151 \times 101 \times 256$	10^8	0.50	300	32.06 ± 0.24	0.7
$271 \times 151 \times 256$	10^8	1.00	150	32.21 ± 0.32	1.0
$271 \times 151 \times 256$	10^8	1.25	150	31.77 ± 0.15	0.5
$321 \times 161 \times 256$	10^8	1.50	150	31.39 ± 0.11	0.3
$321 \times 161 \times 256$	10^8	1.75	249	31.57 ± 0.10	0.3
$361 \times 181 \times 256$	10^8	2.00	145	31.25 ± 0.31	1.0
$401 \times 201 \times 256$	10^8	2.25	143	31.25 ± 0.21	0.7
$401 \times 201 \times 256$	10^8	2.50	146	31.87 ± 0.18	0.6
$401 \times 201 \times 256$	10^8	2.75	145	32.34 ± 0.08	0.3
$451 \times 225 \times 256$	10^8	3.00	141	32.29 ± 0.12	0.4
$541 \times 257 \times 256$	10^8	4.00	132	33.20 ± 0.08	0.2
$801 \times 451 \times 256$	10^8	8.00	81	34.78 ± 0.13	0.4
$201 \times 101 \times 310$	10^9	0.50	150	63.67 ± 0.56	0.9
$361 \times 181 \times 310$	10^9	1.00	139	64.31 ± 0.64	1.0
$811 \times 321 \times 310$	10^9	2.00	109	63.25 ± 0.26	0.4
$1025 \times 551 \times 310$	10^9	3.00	110	65.11 ± 0.50	0.8

TABLE 1. Parameters of simulation runs. The grid resolution, Rayleigh number Ra and aspect ratio Γ are given. The Prandtl number is $Pr = 0.7$ throughout this study. Furthermore, the total integration time in units of the free-fall time $t_f = H/U_f$, with $U_f = \sqrt{g\alpha\Delta T H}$, and the Nusselt number Nu with standard deviation σ are given. For all Rayleigh numbers, we find that a characteristic convective velocity $U_c = \sqrt{\langle u^2 \rangle_{V,t}}$ is about $U_f/5$. Consequently, t/t_f has to be divided by 5 in order to get t/t_c, where the alternative convective time unit is defined as $t_c = H/U_c$. This time unit was suggested by van Reeuwijk, Jonker & Hanjalić (2008) since the standard free-fall velocity U_f is too large in comparison with actual turbulent velocity fluctuations.

horizontal circular plane since the resolution at the sidewalls has to be maintained. The smallest mean scale in a turbulent flow is the Kolmogorov dissipation length which is usually defined as

$$\eta_K = \frac{\nu^{3/4}}{\langle \epsilon \rangle^{1/4}}, \tag{2.4}$$

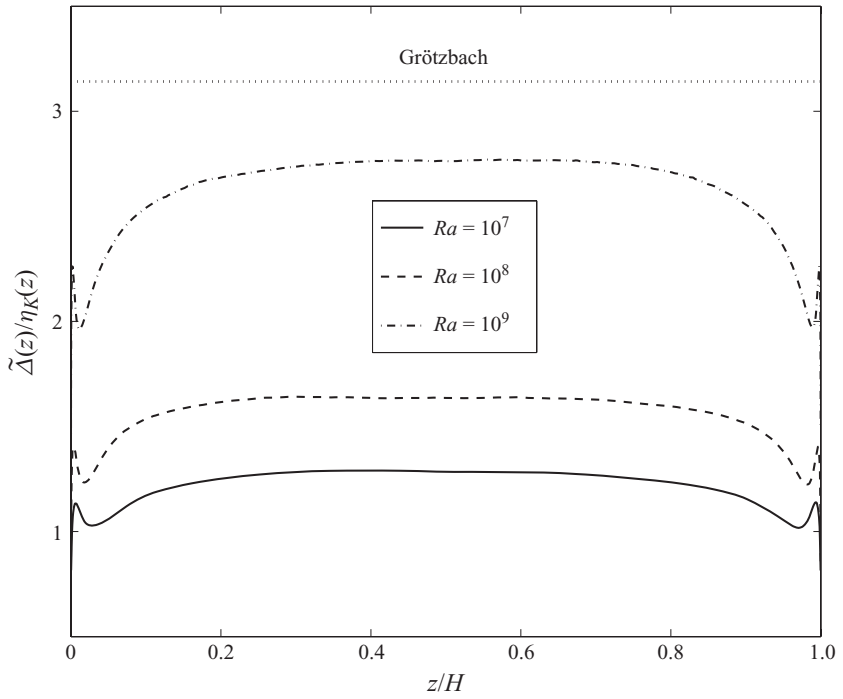

FIGURE 1. Ratio of the maximum geometric mean grid spacing $\tilde{\Delta}(z)$ and the Kolmogorov scale $\eta_K(z)$ for three different Rayleigh numbers in cells with $\Gamma = 1$. The horizontal dotted line indicates the global Grötzbach resolution criterion $\Delta/\eta_K \leqslant \pi$ (Grötzbach 1983) where Δ is the global geometric mean grid spacing.

where $\langle\epsilon\rangle$ is the mean of the energy dissipation rate (see e.g. Pope 2000), which is given by

$$\epsilon(\boldsymbol{x}, t) = \frac{\nu}{2}\left(\frac{\partial u_i}{\partial x_j} + \frac{\partial u_j}{\partial x_i}\right)^2. \tag{2.5}$$

The symbol '$\langle\ \rangle$' stands for a statistical average. The resolution criteria based on η_K works well in homogeneous isotropic turbulence, but has to be modified for the inhomogeneous situation. We define a height-dependent Kolmogorov scale as

$$\eta_K(z) = \frac{\nu^{3/4}}{\langle\epsilon(z)\rangle_{A,t}^{1/4}}. \tag{2.6}$$

The symbol '$\langle\ \rangle_{A,t}$' denotes an average over a plane at a fixed height z and an ensemble of statistically independent snapshots. Following Emran & Schumacher (2008), we define the maximum of the geometric mean of the grid spacing at height z by $\tilde{\Delta}(z) = \max_{\phi,r}[\sqrt[3]{\Delta_\phi(z)\Delta_r(z)\Delta_z(z)}]$. Figure 1 plots the ratios $\tilde{\Delta}(z)/\eta_K(z)$ over the cell height for three different Rayleigh numbers. One can observe that the ratio varies close to the upper and lower plates and levels off in the bulk. Overall, it does not exceed the global resolution criterion by Grötzbach (1983), $\Delta/\eta_K \leqslant \pi$, for the given Rayleigh numbers.

Figure 2 displays the z-dependent mean profiles of the temperature and the product of the temperature and vertical velocity component. The variations manifested in the profiles contribute to the Nusselt number variation with Γ. The inset magnifies the

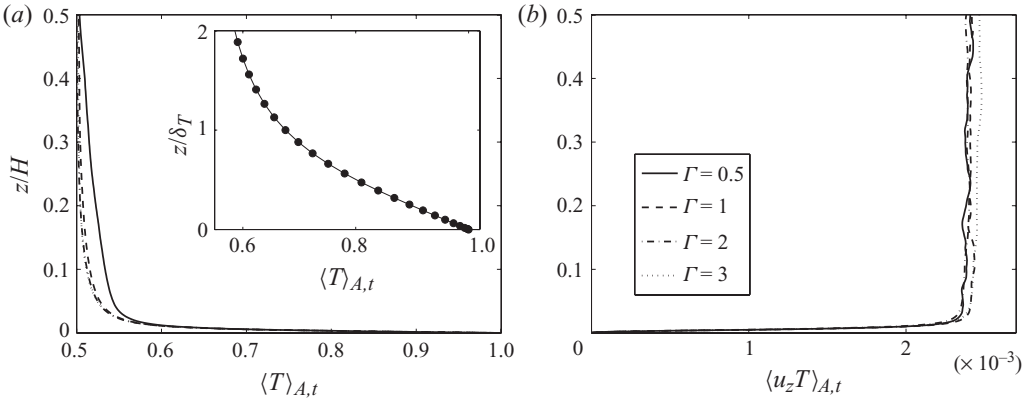

FIGURE 2. The z-dependent mean profiles of the (a) temperature and (b) product of the temperature and vertical velocity component. Data for four aspect ratios are plotted at Rayleigh number $Ra = 10^9$. The inset in (a) magnifies the mean temperature profile in the thermal boundary layer for the simulation at $Ra = 10^9$ and $\Gamma = 3$. Profiles are shown for the lower half ($0 \leqslant z/H \leqslant 0.5$) of the cell only due to symmetry.

mean temperature profile for $Ra = 10^9$ and $\Gamma = 3$, where the boundary layer is resolved with 17 grid planes.

3. Dependence of the global heat transfer on aspect ratio

3.1. $Nu(\Gamma)$ at fixed Rayleigh number Ra

The heat transfer through each plane at a fixed height z following the averaging of (2.3) with respect to the horizontal plane is given by

$$Nu(z) = \frac{\langle u_z T\rangle_{A,t} - \kappa \partial_z \langle T\rangle_{A,t}}{\kappa \Delta T/H} = \text{const.} \tag{3.1}$$

The global Nusselt number Nu can then be written as

$$Nu = \frac{1}{H}\int_0^H Nu(z)\mathrm{d}z = 1 + \frac{H}{\kappa \Delta T}\langle u_z T\rangle_{V,t}, \tag{3.2}$$

where '$\langle\ \rangle_{V,t}$' denotes an average over the whole cell volume and an ensemble of statistically independent snapshots. The samples are gathered over the total integration time, which is also listed in table 1, and given in units of the free-fall time $t_f = H/U_f$, with the free-fall velocity $U_f = \sqrt{g\alpha\Delta T H}$ as the characteristic velocity. The last columns of the table display the Nusselt number Nu and the standard deviation σ, which is calculated as

$$\sigma = \sqrt{\frac{1}{N_z}\sum_{j=1}^{N_z}[Nu(z_j) - Nu]^2}\,. \tag{3.3}$$

Here z_j is the vertical coordinate of each gridplane and $Nu(z)$ and Nu follow from (3.1) and (3.2), respectively. These standard deviations are smaller than or equal to 1 % and thus comparable with Kerr (1996). The total integration time of the simulations is comparable with van Reeuwijk, Jonker & Hanjalić (2008).

Figure 3 shows the Nusselt number Nu as a function of the aspect ratio Γ for three different Rayleigh numbers, namely $Ra = 10^7, 10^8$ and 10^9. At $Ra = 10^7$ (figure 3a),

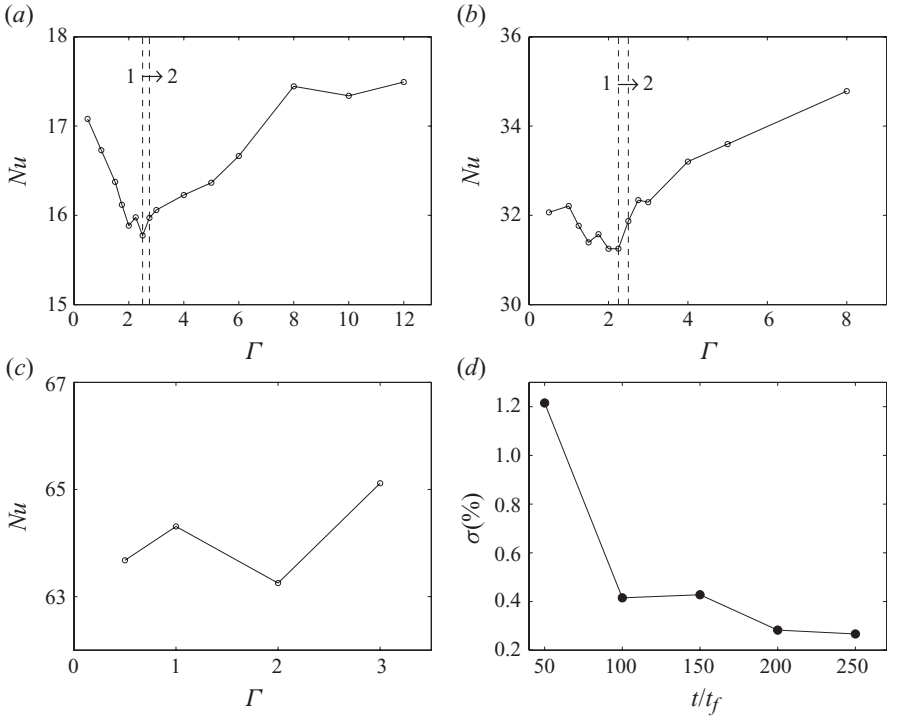

FIGURE 3. Nusselt number Nu as a function of the aspect ratio Γ for (a) $Ra = 10^7$, (b) $Ra = 10^8$, (c) $Ra = 10^9$. The crossover from one circulation roll to two rolls is indicated in (a) and (b) by two parallel dashed lines. The errorbars for all Nusselt numbers shown are smaller than the size of the symbols. For each single snapshot, the Nusselt number was determined as a volume average. In addition, an arithmetic mean is taken over $N_{samp} = t/t_f$ statistically independent turbulent samples (see (3.2) and table 1). The decrease of the standard deviation σ with increasing number of samples $N_{samp} = t/t_f$ is shown in (d) for the data set $Ra = 10^7$ and $\Gamma = 2$.

Nu decreases with increasing Γ, attains a minimum value at $\Gamma \approx 2.5$, then increases to a maximum value close to $\Gamma \approx 8$, and finally saturates for $\Gamma > 8$. Variations of $Nu(\Gamma)$ can also be observed in figures 3(b) and 3(c) for the other two larger Rayleigh numbers. The minimum of $Nu(\Gamma)$ is detected at $\Gamma \approx 2.5$ and $\Gamma \approx 2.25$ for $Ra = 10^7$ and $Ra = 10^8$, respectively. This is the point where a transition in the LSC from a single-roll to a double-roll pattern will occur (see § 4). On the basis of stability analysis, Oresta *et al.* (2007) have shown that there is always a single roll for $\Gamma \leqslant 2$ in the weakly nonlinear regime irrespective of the initial conditions. However, our Rayleigh numbers here are in fully turbulent regime. With our present computing capability, we could not go beyond $\Gamma > 8$ for $Ra = 10^8$ and $\Gamma > 3$ for $Ra = 10^9$. In particular, for the largest Rayleigh number, we can provide four data points only and, therefore, the minimum of $Nu(\Gamma)$ is inconclusive in this case, although it is apparently at $\Gamma \approx 2$ in figure 3(c). On the basis of our simulation data, we cannot conclude exactly at which aspect ratio the Nusselt numbers become independent of the cell geometry for all the Rayleigh numbers; however, the trend indicates that it is at $\Gamma \approx 8$ for $Ra = 10^7$ and $\Gamma \gtrsim 8$ for $Ra = 10^8$. The variations in Nu, as defined by the difference between the maximum and minimum in the Nusselt number series, are

significant – especially for the lower Rayleigh numbers – and yield 10.9 %, 11.3 % and 3.0 % for $Ra = 10^7$, 10^8 and 10^9, respectively.

A closer inspection of figure 3(*a–c*) reveals non-monotonic graphs of $Nu(\Gamma)$ with local maxima and minima, in particular for the two larger Rayleigh numbers. We have first verified that there is sufficient statistical convergence of the data (see table 1). Since statistical uncertainties can be excluded, there must be physical reasons for the behaviour observed in figure 3. We observe that the time-averaged flow patterns in the turbulent cell are similar to those at the onset of convection (figures 5 and 6). In this case, an integer number of rolls must fit into the cell. This is exactly the reason why, for example, the linear instability studies by Koschmieder (1969) and Charlson & Sani (1970, 1971) in the cylindrical cells with insulated sidewalls yield stability curves $Ra_{cr}(\Gamma)$ with local extrema in the low-Γ regime, and extend to an asymptotic value for larger Γ only. Small discontinuities in $Nu(Ra)$ in the weakly nonlinear regime, which could be traced back to a change of the number of rolls in the cell, have been also reported by Gao *et al.* (1987).

These pattern bifurcations can be studied when a small number of degrees of freedom dominates the dynamics. It is not obvious that in a fully turbulent case, where infinitely many degrees of freedom exist, coherent patterns exist and prevail. Similar patterns can, however, be found in a turbulent Taylor vortex flow at high Reynolds number (Lathrop *et al.* 1992). The POD analysis in § 5 demonstrates that the LSC carries a significant amount of heat through the cell. We also show that a change of the LSC morphology causes jumps in the amount of heat transported by the first few POD modes. These findings strengthen our observation of Γ-dependent heat transfer (see figure 3). It should also be mentioned that persistent coherent patterns at larger Rayleigh numbers have been emphasized by Busse (2003) as a sequence-of-bifurcations to the turbulent state.

3.2. $Nu(Ra)$ at fixed aspect ratio Γ

Systematic experiments with various values of Γ larger than unity were conducted by three groups. First, Wu & Libchaber (1992) detected a power law scaling with Ra, namely

$$Nu(Ra, \Gamma) = A(\Gamma) \times Ra^{\beta}. \tag{3.4}$$

Their measurements indicated almost an unchanged exponent β and an aspect-ratio-dependent prefactor. Second, Sun *et al.* (2005) suggested the following scaling law on the basis of their experiments as

$$Nu(Ra, \Gamma) = A_1(\Gamma) \times Ra^{\beta_1} + A_2(\Gamma) \times Ra^{\beta_2}. \tag{3.5}$$

This scaling is a combination of two power laws with $\beta_1 = 1/3$ and $\beta_2 = 1/5$. Again, the prefactors depend on Γ and a saturation of the Nusselt number Nu for $\Gamma \geqslant 10$ has been detected. Third, Funfschilling *et al.* (2005) did not observe any sensitivity of the heat transfer on the aspect ratio. Their measurements gave power laws of the form

$$Nu(Ra, \Gamma) = A \times Ra^{\beta}, \tag{3.6}$$

but with a continuous drift of the exponent from $\beta = 0.28$ at $Ra \sim 10^8$ up to $\beta = 0.33$ at $Ra \gtrsim 10^{10}$. Their results were essentially unaltered by an increase in the aspect ratio. On the numerical side, a power law of $Nu \sim \Gamma^{-1}$ for $\Gamma \leqslant 3$ was obtained by Ching & Tam (2006) on the basis of two-dimensional steady-state calculations.

The present data allows us to compare our results with the scaling laws given in (3.4)–(3.6). Table 2 displays the fit results for power laws in the form $Nu = A \times Ra^{\beta}$

Fit coefficients	$\Gamma = 1/2$	$\Gamma = 1$	$\Gamma = 2$	$\Gamma = 3$
A	0.165	0.145	0.127	0.118
β	0.287	0.294	0.300	0.305

TABLE 2. Nusselt number as a function of the Rayleigh number for different aspect ratios. The scaling $A \times Ra^{\beta}$ has been fit for four aspect ratios.

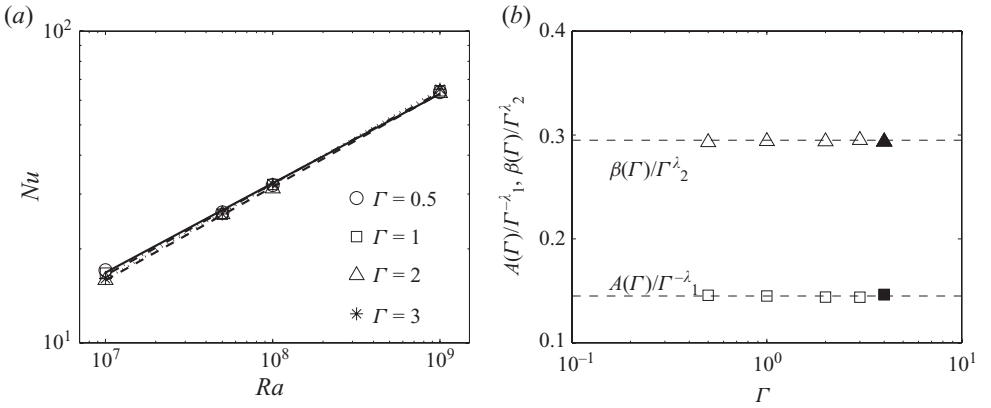

FIGURE 4. Aspect ratio dependence of the fit coefficients, $A(\Gamma)$ and $\beta(\Gamma)$. (a) Data for the Nusselt number and power law fits to $Nu(Ra)$ as reported in table 2. (b) Compensated power law plots for $A(\Gamma)$ and $\beta(\Gamma)$. The exponents are $\lambda_1 = 0.18$ for A and $\lambda_2 = 0.03$ for β. The open symbols are the present simulation data. The filled symbols correspond to Niemela & Sreenivasan (2006). We have fitted their data from $Ra = 1.10 \times 10^8$ to 9.51×10^9 (see table 1 in Niemela & Sreenivasan 2006).

at fixed aspect ratios $\Gamma = 1/2, 1, 2$ and 3. Each data series contains four Rayleigh numbers, namely $Ra = 10^7$, 5×10^7, 10^8 and 10^9. Within this range of Ra, we observe a growth of the exponent β from 0.287 to 0.305, which is about 6 % variation. The present scaling law for $\Gamma = 1$ differs slightly from the earlier reported scaling of $Nu = 0.175 \times Ra^{0.283}$ in Emran & Schumacher (2008). In the former case, six Rayleigh numbers from 5×10^6 to 10^9, but fewer snapshots for the higher Rayleigh numbers, were included. This demonstrates the sensitivity of the scaling laws and demands additional efforts to be taken here. Both the prefactor A and exponent β seem to be functions of the aspect ratio and the functional form is thus

$$Nu(Ra, \Gamma) = A(\Gamma) \times Ra^{\beta(\Gamma)}. \tag{3.7}$$

Figure 4(a) shows power law fits (3.7) to our DNS data for several aspect ratios and figure 4(b) shows $A(\Gamma) \sim \Gamma^{-\lambda_1}$ and $\beta(\Gamma) \sim \Gamma^{\lambda_2}$ in a compensated form for $0.5 \leqslant \Gamma \leqslant 3$. The measurements that come closest to the present study, both in Rayleigh and Prandtl numbers, are those by Niemela & Sreenivasan (2006) at $\Gamma = 4$. A power law fit of their data for $1.10 \times 10^8 \leqslant Ra \leqslant 9.51 \times 10^9$ yields $Nu = 0.114 \times Ra^{0.306}$. Adding these parameters to figure 4 covers data over almost a decade of Γ. We see that both parameters, A and β, almost perfectly follow the power law with respect to Γ. The exponent for β is $\lambda_2 = 0.03$, which is small. The dependence of the prefactor A on Γ is stronger, with $\lambda_1 = 0.18$. It is clear that further studies are required to determine whether this weak dependence on Γ prevails at larger Rayleigh numbers or not. Furthermore, we can expect that, for sufficiently

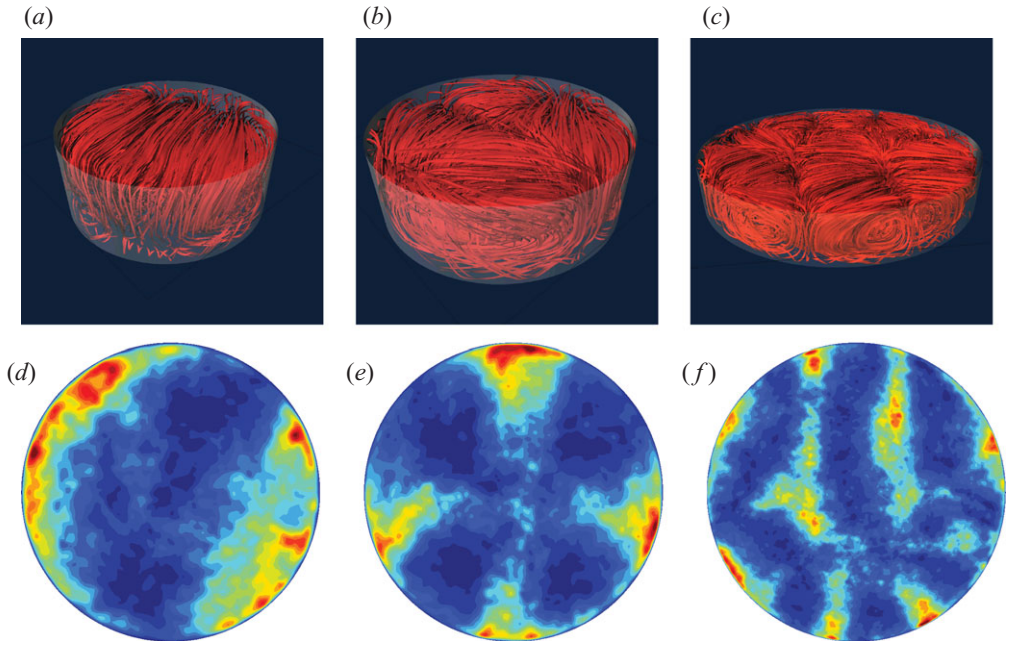

FIGURE 5. Flow patterns at different aspect ratios. Streamlines (*a–c*) and contours of the local heat transfer $u_z\theta$ (*d–f*) for three different aspect ratios, $\Gamma = 2.5$ (*a*, *d*), $\Gamma = 3$ (*b*, *e*) and $\Gamma = 6$ (*c*, *f*), at $Ra = 10^7$ are presented. All data are obtained by time averaging a sequence of 50 statistically independent snapshots. In the bottom row $\langle u_z\theta\rangle_t(r, \phi, z = 1/2)$ is shown.

large Γ, both exponents will saturate to aspect-ratio-independent values. This was shown clearly in figure 3 for $Ra = 10^7$. In addition, the saturation threshold for A and β most likely depends on the Prandtl number, which is constant in our case.

4. Large-scale circulation

Let us now investigate the behaviour of the LSC. In figure 5, we present the LSC for three aspect ratios $\Gamma = 2.5$, 3 and 6 at $Ra = 10^7$. The streamline plots in the upper three panels have been obtained by averaging the velocity field over 50 consecutive snapshots. These snapshots are separated from each other by $\Delta t = t_f = H/U_f$. Averaging over three disjoint sequences of 50 snapshots leaves the observed LSC patterns unchanged. We conclude, therefore, that the detected LSC pattern is not transient. Transient behaviour and large-scale saturation have been investigated by von Hardenberg *et al.* (2008). The time averaging over the coarse sequence of snapshots removes not only all small-scale fluctuations of the velocity field, but also oscillations of the LSC, which have been observed in recent experiments (e.g. Brown & Ahlers 2008; Xi & Xia 2008*a*), mostly for $\Gamma \leqslant 1$. Between $\Gamma = 2.5$ and 2.75, the system bifurcates from a one-roll to a two-roll pattern. We have also identified this crossover in LSC between $2.25 < \Gamma < 2.5$ for $Ra = 10^8$. However, for $Ra = 10^9$ we have noticed a single-roll circulation pattern at $\Gamma = 2$ and a triple-roll pattern at $\Gamma = 3$. Here, the LSC patterns for aspect ratios between 2 and 3 were not investigated for the highest Rayleigh number. A single roll at $\Gamma = 2$ is consistent with the findings of Sun *et al.* (2005), Oresta *et al.* (2007) and Bukai *et al* (2009). The crossovers of the LSC are marked in figures 3(*a*) and 3(*b*) by two parallel dashed lines. With

increasing aspect ratio, the LSC becomes a more complex multi-roll configuration, as can be seen in the third column of figure 5 for $\Gamma = 6$.

In the lower row of figure 5, we show the corresponding contour plots of $\langle u_z\theta\rangle_t$ at the midplane where

$$\theta(\boldsymbol{x}, t) = T(\boldsymbol{x}, t) - \langle T(z)\rangle_{A,t}. \tag{4.1}$$

The quantity $u_z\theta$ is the local convective heat flux contribution and $u_z\theta > 0$ if rising and falling plumes are present. The appearance of rising and falling plumes (red in $\langle u_z\theta\rangle_t$ contours) in figure 5(*d–f*) is directly correlated to the corresponding LSC pattern of the time averaged velocity field. We have also verified that almost the same pattern holds for the fluctuations of the local heat transfer, as given by $\langle (u_z\theta)^2\rangle_t$.

As already indicated in figure 5, the LSC becomes more complex when the aspect ratio becomes larger. For Rayleigh number 10^7, we were able to run a numerical simulation up to $\Gamma = 12$. Figure 6 reveals such a complex LSC pattern in convective flow for two different Rayleigh numbers, $Ra = 10^7$ and $Ra = 6000$, at $\Gamma = 12$. Figure 6(*a*, *c*) shows the top view of the streamlines for instantaneous snapshots of both simulations, while figure 6(*b*, *d*) shows the time-averaged velocity field as in figure 5. When the small-scale turbulence (see figure 6*c*) is filtered out, the resulting pattern is strikingly similar to the weakly nonlinear regime right above the onset of convection. We observe extended rolls and pentagon-like cells. These patterns have been reported, for example, in experiments by Croquette (1989) with argon at $Pr = 0.69$ for Rayleigh numbers $Ra \approx 2Ra_c$, where Ra_c is the critical Rayleigh number of the onset of convection. Figure 7 adds further support to the Rayleigh-number-dependence of the LSC. Figure 7(*a*) nicely displays the extended roll patterns in the weakly nonlinear regime at $Ra = 6000$ and $\Gamma = 8$. Relics of these patterns are still present in the turbulent regime at $Ra = 10^7$ (figure 7*b*). For the largest Rayleigh number, $Ra = 10^8$, the LSC is transformed into a pentagon-like cell structure. Similarly, if we compare figure 6(*b*) with figure 7(*a*), we see that there is a reorganization of flow from the roll shape to pentagonal or hexagonal structures with increasing Γ for a fixed Ra.

Regular patterns in the turbulent convection regime were studied in detail by Fitzjarrald (1976) in a square cell filled with air for aspect ratios between 2 and 58 covering a range of Rayleigh numbers between 4×10^4 and 7×10^9. He calculated the dominant horizontal scales from the Fourier co-spectra of u_z and T. The spectral peak in the heat flux corresponds to a wavelength Λ that increased from $4H$ to $6H$ for $4\times10^4 < Ra < 1.7\times10^7$ and thus $58 > \Gamma > 15$. Based on figures 5 and 6 for $Ra = 10^7$ and figure 7 for $Ra = 10^8$, we take the width of the LSC roll (which corresponds to the spacing between local maxima of $\langle u_z\theta\rangle$) as $\Lambda/2$ and get thus a wavelength $\Lambda \approx 4H$ for $\Gamma = 6, 8$ and 12. The associated wavenumber $k = 2\pi/\Lambda \approx 1.5H^{-1}$ which is about half the size of $k_c = 3.117H^{-1}$ at the onset of thermal convection in an infinite layer. The dominant horizontal scales are similar to those of Fitzjarrald. The results in figure 5 further confirm the observation made by Fitzjarrald. This wavelength shrinks at smaller aspect ratios where the pattern has to fit into the cylindrical cell. Hartlep *et al.* (2005) have also traced back their large-scale turbulent temperature patterns to the states which are observed in the weakly nonlinear regime. A series of simulations at $\Gamma = 10$ for Rayleigh numbers up to $Ra = 10^7$ confirms a characteristic wavelength of half their box size, i.e. $\Lambda \approx 5H$ for $Pr = 0.7$. This wavelength was $\Lambda \approx 3H$ at $Ra = 4000$. Their study shows in addition a clear shape dependence of the circulation rolls on the Prandtl number. Slight variations of Λ in the three studies might be caused by different cell geometries and boundary conditions

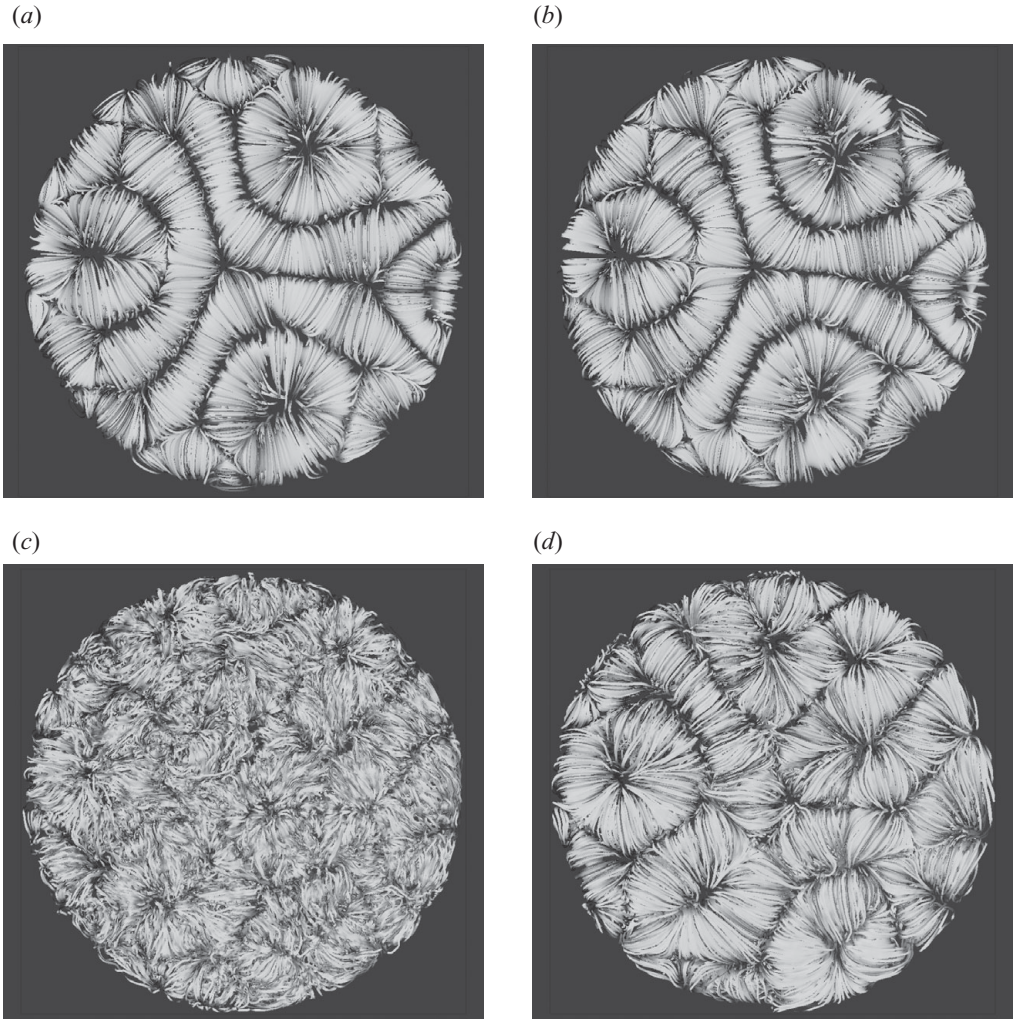

FIGURE 6. Top view of the LSC patterns at $\Gamma = 12$ for two different Rayleigh numbers, $Ra = 6 \times 10^3$ (*a*, *b*) and $Ra = 10^7$ (*c*, *d*). The streamlines of the instantaneous (*a*, *c*) and time-averaged (*b*, *d*) velocity field are shown here. In both cases, the time averaging is done over 50 convective time units t_f.

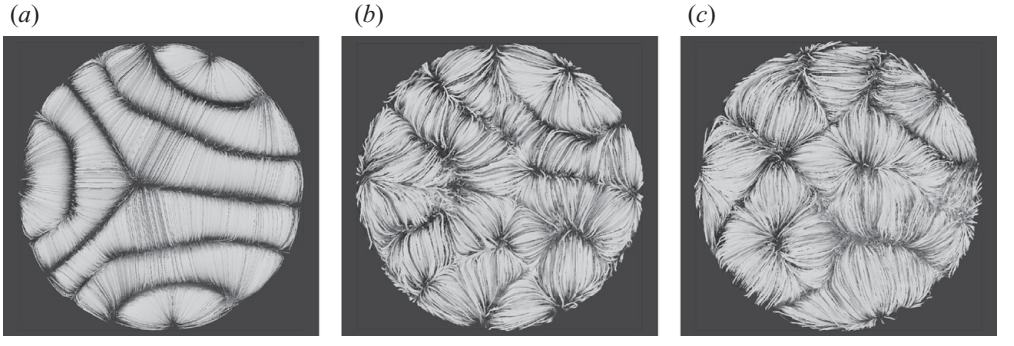

FIGURE 7. Rayleigh number dependence of the LSC: (*a*) $Ra = 6000$, (*b*) $Ra = 10^7$ and (*c*) $Ra = 10^8$. All data are for $\Gamma = 8$.

in the simulations. Nevertheless, the same range of wavelengths can be observed for $Ra \sim 10^7$ and $Pr = 0.7$ in all works.

Although qualitative similarities between the LSC patterns at small Ra and those at higher Ra are obvious from figure 6, we can expect that the particular mechanisms that drive the large-scale flow will be different. The onset of a flow motion for small Ra is triggered by a slight dominance of buoyancy forces per unit mass, $f_b = g\alpha\theta$, compared to the restoring drag forces per unit mass, $f_d = (1/2)C_f u_z^2 H$. This is the simple chaotic waterwheel picture by Malkus and Howard (see Strogatz 1994). In the turbulent case, the heat transport through the thin thermal boundary layers is responsible for large-scale spatial temperature differences. Spatial temperature differences create pressure gradients which drive the large-scale flow (Reeuwijk *et al.* 2008). This might the reason why the wavelength of the circulation rolls is slightly increasing with growing Ra.

We can summarize that, for the range of parameters covered here, the LSC patterns do not disappear in the turbulent regime up to $Ra = 10^9$. For the larger aspect ratios pentagon-like circulation cells are formed preferentially.

5. Proper orthogonal decomposition of the turbulent convection flow

5.1. *The snapshot method*

The turbulent heat transfer is the sum of transfers by the LSC and the turbulent fluctuations. In order to disentangle both contributions systematically, we conduct a so-called Karhunen–Loève method or proper orthogonal decomposition. The reader is referred to Smith, Moehlis & Holmes (2005) for a compact tutorial on this subject. Here, we outline the basic ideas only. The application of the POD method to the convection problem goes primarily back to Sirovich and his co-workers (see e.g. Sirovich & Park 1990). Consider a state vector $\boldsymbol{v} = (\boldsymbol{u}, \theta)$ with zero mean, $\langle \boldsymbol{v} \rangle = 0$. It has a mean turbulent energy (kinetic energy plus temperature variance), which is given by

$$E = \langle (\boldsymbol{v}, \boldsymbol{v}) \rangle = \left\langle \int_V \sum_{k=1}^{4} v_k(\boldsymbol{x}, t) v_k(\boldsymbol{x}, t) \, \mathrm{d}^3 x \right\rangle_t , \tag{5.1}$$

where V is the cell volume and the scalar product $(\cdot, \cdot)$ is defined in $L_2(V)$. At the core of the method is the determination of the POD modes $\boldsymbol{\phi}(\boldsymbol{x})$, which maximize the following functional

$$\frac{\langle |(\boldsymbol{v}, \boldsymbol{\phi})|^2 \rangle_t}{(\boldsymbol{\phi}, \boldsymbol{\phi})} \to \max. \tag{5.2}$$

Variational calculus then yields the following integral equation

$$\int_V \hat{\boldsymbol{K}}(\boldsymbol{x}, \boldsymbol{x}') \boldsymbol{\phi}^{(m)}(\boldsymbol{x}') \, \mathrm{d}^3 x' = \lambda_m \boldsymbol{\phi}^{(m)}(\boldsymbol{x}), \tag{5.3}$$

with the kernel (or covariance matrix) $K_{ij}(\boldsymbol{x}, \boldsymbol{x}') = \langle v_i(\boldsymbol{x}, t) v_j(\boldsymbol{x}', t) \rangle_t$ and $i, j = 1, 2, 3, 4$. If the kernel is a Hermitian and non-negative operator, the set of empirical eigenfunctions $\{\boldsymbol{\phi}^{(m)}\}$ forms an orthonormal system, i.e. $(\boldsymbol{\phi}^{(m)}, \boldsymbol{\phi}^{(n)}) = \delta_{mn}$. The integral equation is transformed into a matrix eigenvalue problem. In our case the size of the kernel becomes extremely large, namely a $4N \times 4N$ matrix for $\boldsymbol{v} = (\boldsymbol{u}, \theta)$ and $N = N_r \times N_\phi \times N_z$. Symmetries and incompressibility of the flow reduce the number of degrees of freedom in many cases. However, we still have to apply the method of snapshots, which is the preferred choice if $N \gg N_T$, with N_T the number of snapshots.

We therefore construct empirical eigenfunctions as a linear combination of the state vectors $\boldsymbol{v}$, where the eigenfunctions are given by

$$\boldsymbol{\phi}^{(m)}(\boldsymbol{x}) = \sum_{i=1}^{N_T} \alpha_i^{(m)} \boldsymbol{v}(\boldsymbol{x}, t_i)\,. \tag{5.4}$$

Such a procedure reduces the complexity of the problem and leads to the solution of an eigenvalue problem of $N_T \times N_T$ matrix, as is evident from the subsequent expressions. If $\langle\ \rangle_t$ is substituted by an arithmetic mean over the snapshots, it follows from (5.3) that

$$\frac{1}{N_T} \int_V \sum_{k=1}^{N_T} v_p(\boldsymbol{x}, t_k) v_n(\boldsymbol{x}', t_k) \phi_n^{(m)}(\boldsymbol{x}')\, \mathrm{d}^3 x' = \lambda_m \phi_p^{(m)}(\boldsymbol{x}). \tag{5.5}$$

With (5.4) one can arrive at

$$\sum_{k=1}^{N_T} v_p(\boldsymbol{x}, t_k) \left[\sum_{i=1}^{N_T} \frac{1}{N_T} \int_V v_n(\boldsymbol{x}', t_k) v_n(\boldsymbol{x}', t_i)\, \mathrm{d}^3 x'\, \alpha_i^{(m)} \right] = \sum_{q=1}^{N_T} v_p(\boldsymbol{x}, t_q) \lambda_m \alpha_q^{(m)}\,, \tag{5.6}$$

and thus

$$\sum_{i=1}^{N_T} \frac{1}{N_T} (\boldsymbol{v}(t_k), \boldsymbol{v}(t_i)) \alpha_i^{(m)} = \sum_{i=1}^{N_T} C_{ki} \alpha_i^{(m)} = \lambda_m \alpha_k^{(m)}\,. \tag{5.7}$$

Eventually, N_T eigenvectors $\{\boldsymbol{\alpha}^{(m)}\}$, with $m = 1, 2, \ldots, N_T$, represent N_T POD modes $\{\boldsymbol{\phi}^{(m)}\}$ (vectors of $4N$ components) constructed from the state vectors.

We proceed in two different steps. First, we use $\boldsymbol{v} = \boldsymbol{u}$ only and not the combined velocity–temperature state vectors. The eigenvalue spectrum $E_1 \geqslant E_2 \geqslant \ldots E_{N_T}$ then quantifies the fraction of the turbulent kinetic energy contained in each of the N_T POD modes. Second, we use $\boldsymbol{v} = (\boldsymbol{u}, \theta)$ and determine the total energy spectrum $\lambda_1 \geqslant \lambda_2 \geqslant \ldots \lambda_{N_T}$. The latter will be used in the subsequent sections. Both eigenvalue spectra are presented in figure 8 for different Rayleigh numbers and $N_T = 100$ snapshots. At the smallest Rayleigh number $Ra = 6 \times 10^3$, the first few POD modes contain most of the total energy (figure 8*a*) and kinetic energy (Figure 8*b*). This is the weakly nonlinear regime of convection. With increasing Rayleigh number, the spectra decay slowly. For Rayleigh numbers $Ra \geqslant 10^7$ the convection is turbulent and a significant fraction of the kinetic and total energy is distributed among the higher-order POD modes. The inset in Figure 8(*a*) shows the magnified view for the first few POD modes. This observation is in agreement with Sirovich & Park (1990). The dynamic significance of the subsequent modes increases steadily with increasing Rayleigh number since turbulent fluctuations are present.

5.2. *Spatial structure of primary and secondary modes*

Before we proceed to the analysis of the turbulent heat transfer, we visualize the spatial structure of the first two POD modes and compare it with the LSC. Figure 9 shows the three-dimensional view of the primary and secondary modes. The velocity field $(\phi_1^{(m)}(\boldsymbol{x}), \phi_2^{(m)}(\boldsymbol{x}), \phi_3^{(m)}(\boldsymbol{x}))$, with $m = 1, 2$, is plotted as streamlines in figure 9(*a*, *c*) and the temperature field $\phi_4^{(m)}(\boldsymbol{x})$ at two isolevels is plotted in figure 9(*b*, *d*). The data set corresponds to $\Gamma = 3$ and $Ra = 10^7$. The structure of the velocity field of the primary mode almost exactly replicates the time-averaged velocity field shown in figure 5. This replication is also verified for other aspect ratios, which are not shown here. The shape of the primary temperature POD mode indicates hot up- and

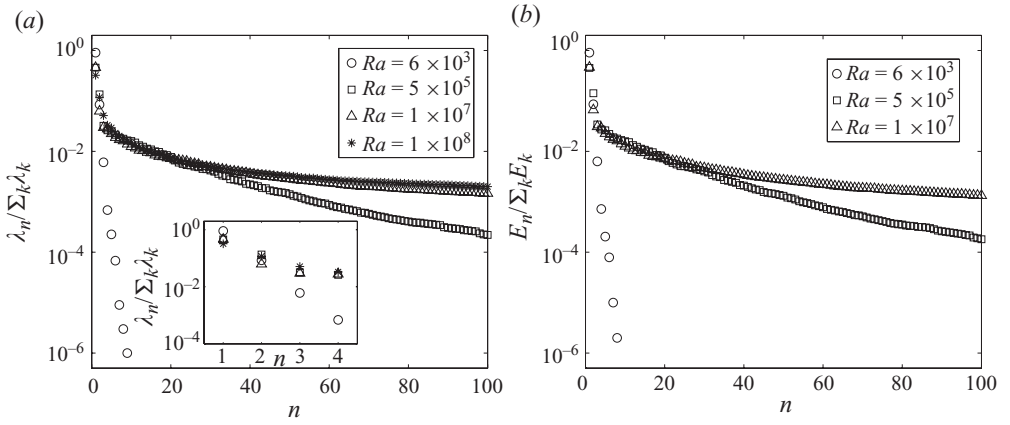

FIGURE 8. (*a*) Normalized POD eigenvalue spectrum of the total energy (thermal plus kinetic) is shown for four different Rayleigh numbers as indicated in the legend. (*b*) Normalized POD eigenvalue spectrum of the kinetic energy is shown for three different Rayleigh numbers as indicated in the legend. The snapshot method was conducted over 100 state vectors. The aspect ratio is $\Gamma = 3$ in all four cases. The spectra for the same Rayleigh number in (*a*) and (*b*) coincide almost perfectly. The inset magnifies the spectra for the first few modes.

cold downwellings on the sidewall. Figure 9(*c*, *d*) shows that the secondary modes exhibit a more complex structure. The primary and secondary POD mode have the same number of large-scale rolls. In addition, we detect smaller substructures of the secondary modes, such as recirculation vortices close to the top and bottom plates and weak modulations of the large-scale rolls.

5.3. *Heat transfer by different POD modes*

The contribution of different subsets of the POD modes to the turbulent heat transfer is determined as follows. We can decompose turbulent snapshots as

$$u_i(\boldsymbol{x}, t) = \sum_{m=1}^{N_T} a_m(t)\phi_i^{(m)}(\boldsymbol{x}), \tag{5.8}$$

$$\theta(\boldsymbol{x}, t) = \sum_{m=1}^{N_T} a_m(t)\phi_4^{(m)}(\boldsymbol{x}), \tag{5.9}$$

with $i = 1, 2, 3$ (or x, y, z). The coefficients $a_m(t)$ correspond to the projection of the turbulent flow field at time t to mode $\boldsymbol{\phi}^{(m)}(\boldsymbol{x})$, which are calculated from the scalar product in $L_2(V)$. The Nusselt number definition (3.2) then translates to

$$\begin{aligned} Nu(N_T) &= 1 + \frac{H}{\kappa \Delta T} \sum_{m,n=1}^{N_T} \left\langle a_m(t)\phi_3^{(m)}(\boldsymbol{x}) \left[\overline{T}(z) + a_n(t)\phi_4^{(n)}(\boldsymbol{x})\right] \right\rangle_{V,t} \\ &= 1 + \frac{H}{\kappa \Delta T} \sum_{m,n=1}^{N_T} \left\langle a_m(t)\phi_3^{(m)}(\boldsymbol{x}) a_n(t)\phi_4^{(n)}(\boldsymbol{x}) \right\rangle_{V,t} \\ &= 1 + \frac{H}{\kappa \Delta T} \sum_{m=1}^{N_T} \lambda_m \left\langle \phi_3^{(m)}(\boldsymbol{x})\phi_4^{(m)}(\boldsymbol{x}) \right\rangle_{V}, \end{aligned} \tag{5.10}$$

where $\overline{T}(z) = \langle T(z) \rangle_{A,t}$. The contribution of the mean profile drops out.

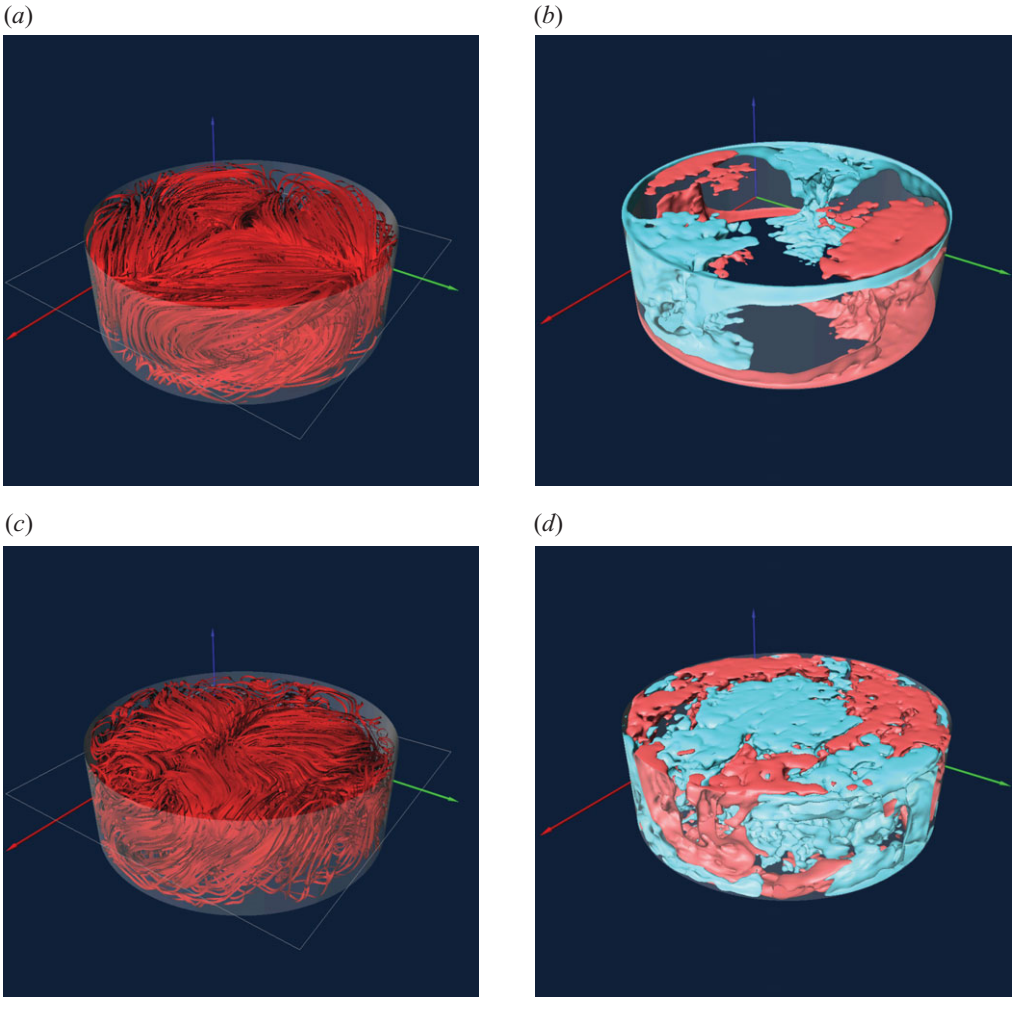

FIGURE 9. Three-dimensional visualization of the first two POD modes for $Ra = 10^7$ and $\Gamma = 3$. (a, b) Streamlines of the primary flow mode ($\phi_1^{(1)}, \phi_2^{(1)}, \phi_3^{(1)}$) (figure 9$a$) and isosurfaces of the primary temperature mode $\phi_4^{(1)}$ (figure 9b) at the isolevels $\pm 0.5\Delta T$. (c, d) Streamlines of the secondary flow mode ($\phi_1^{(2)}, \phi_2^{(2)}, \phi_3^{(2)}$) (figure 9$c$) and isosurfaces of the secondary temperature mode $\phi_4^{(2)}$ (figure 9d) at the isolevels $\pm 0.095\Delta T$. Blue isosurfaces correspond to negative values and red isosurfaces to positive values in both figures.

In figure 10, we report the contribution of various POD modes to the global heat transfer for $Ra = 10^7$ and 10^8. The contribution of the primary and secondary modes is displayed in figures 10(a) and 10(b). The expansion (5.10) is then truncated after 1, 2, 5, 20 and 100 POD modes. Figures 10(c) and 10(d) show the accumulated fraction to the heat transfer for the number of modes as given in the legend of both figures. As a consistency check, we compare the full expansion which is based on 100 snapshots with the Eulerian value as determined in § 3. Computational resources limit the present analysis to $N_T = 100$ since intensive data input and output is required. The values of Nu still deviate slightly from those in table 1. It is found that the convergence is slow in particular for the higher-order modes. The slow convergence was also underlined in figure 3(d). In table 3 we have listed in addition some quantitative details of the

Ra	10^7					10^8				
Γ	0.5	1.0	2.0	2.5	3.0	0.5	1.0	2.0	2.5	3.0
Nu	17.08	16.73	15.88	15.77	16.06	32.06	32.21	31.25	31.87	32.29
$Nu(N_T = 100)$	16.74	16.42	15.28	15.26	15.42	31.13	31.78	30.64	30.88	31.05
$(Nu - Nu(N_T = 100))/Nu$	2.0 %	1.8 %	3.8 %	3.3 %	4.0 %	2.9 %	1.3 %	1.9 %	3.1 %	3.8 %
$(Nu(N_T = 1))/(Nu(N_T = 100))$	30 %	46 %	51 %	47 %	55 %	27 %	47 %	51 %	63 %	41 %

TABLE 3. Turbulent heat transport of POD modes. The Nusselt number Nu of the analysis of the DNS data (taken from table 1) is compared with that obtained from a sequence of $N_T = 100$ snapshots denoted by $Nu(N_T = 100)$. Furthermore, the contribution of the primary mode, $Nu(N_T = 1)$, is compared to the total transport, $Nu(N_T = 100)$.

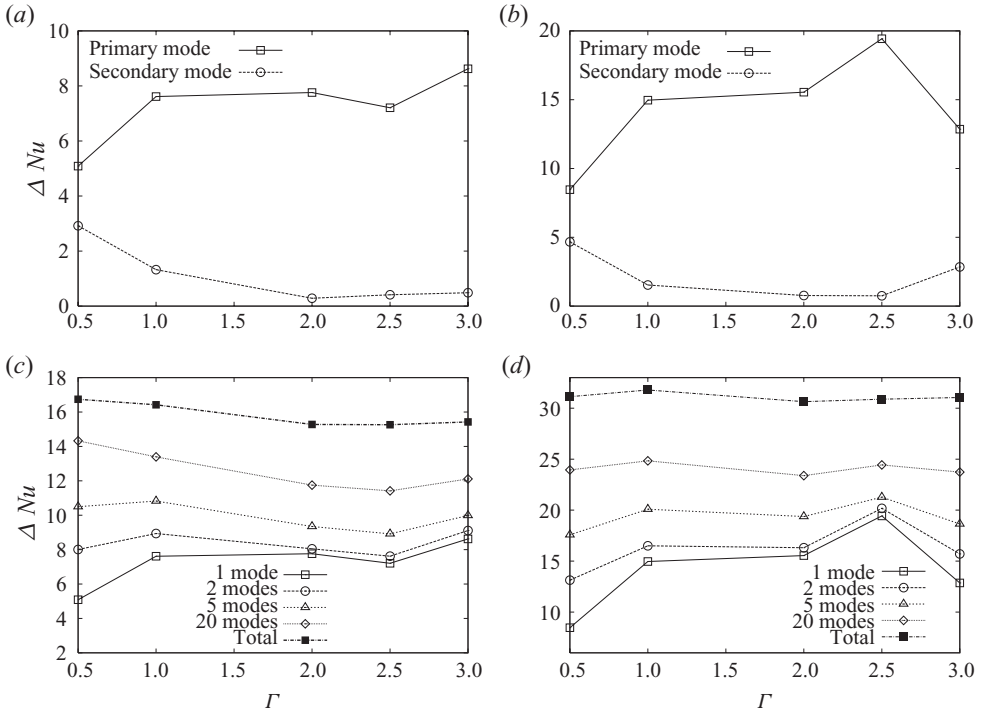

FIGURE 10. Contribution of various POD modes (as indicated in the legend) to the global heat transfer for two Rayleigh numbers and five different aspect ratios. (*a*) Contribution of the primary and secondary modes for $Ra = 10^7$. (*b*) Contribution of the primary and secondary modes for $Ra = 10^8$. (*c*) Accumulated contributions for $Ra = 10^7$. (*d*) Accumulated contributions for $Ra = 10^8$. For completeness we also add the original Eulerian values of the Nusselt number.

POD analysis of the heat transfer. The results are consistent with the Eulerian values in table 1.

The primary POD mode carries the following fraction of the global heat transfer

$$Nu(N_T = 1) = 1 + \frac{\lambda_1 H}{\kappa \Delta T} \left\langle \phi_3^{(1)} \phi_4^{(1)} \right\rangle_V . \tag{5.11}$$

For flow patterns with a single-roll circulation, i.e. $\Gamma = 1$, 2, and 2.5 for $Ra = 10^7$ and $\Gamma = 1$ and 2 for $Ra = 10^8$, the contribution to the heat transfer by the primary POD mode is about the same. It makes up about one-half of the total amount. This

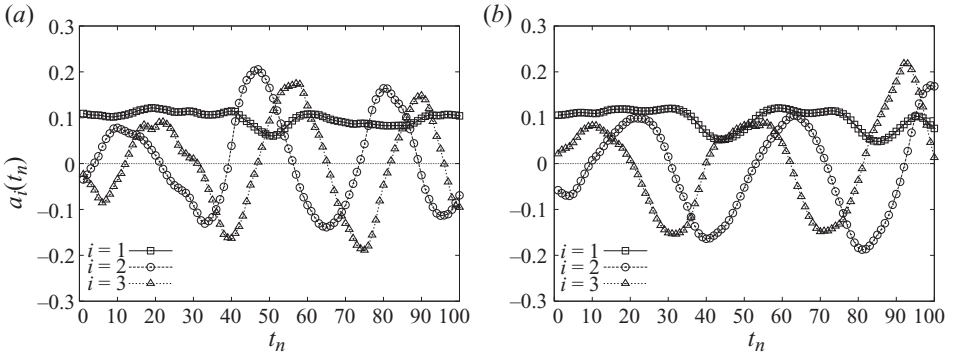

FIGURE 11. Time dependence of $a_i(t)$ for $\Gamma = 2$. The snapshots are therefore projected on the primary ($i = 1$), secondary ($i = 2$) and tertiary mode ($i = 3$). (*a*) $Ra = 10^7$. (*b*) $Ra = 10^8$.

contribution increases by 10 % due to the transition from a single-roll to a double-roll pattern between $\Gamma = 2.5$ and 3 for $Ra = 10^7$. The double-roll LSC can carry more heat through the cell since the number of upwelling and downwelling regions with $\langle u_z\theta\rangle_t > 0$ increases across the cell. This can also be seen in the plots in the lower row of figure 5. One can consider the dynamics around $\Gamma = 2.5$ as a bottleneck for the heat transfer. The one-roll pattern gets ever flatter with increasing Γ and can thus transfer heat less efficiently through the cell. Once the two-roll pattern is established, this bottleneck is removed and the share of the primary mode in the total heat transfer increases. The same transition appears between aspect ratios of 2 and 2.5 for $Ra = 10^8$. Again, we detect a jump of the primary mode contribution by 12 %. The opposite is the case for the slender cell at $\Gamma = 0.5$. One observes a much lower Nu fraction due to the primary mode in comparison to the cases with $\Gamma \geqslant 1$. This can be attributed to the complex flow configuration in the slender cell, in which there are either two counter-rotating rolls on top of each other, or one slender roll (Verzicco & Camussi 2003; Xi & Xia 2008*b*).

The secondary and higher-order modes provide information that can be obtained within the present POD analysis only. The fraction of the secondary POD mode (see figures 10*a* and 10*b*) to the global heat transfer is much smaller than that of the primary. It is about 5 % for the larger aspect ratios and remains almost insensitive when the primary mode switches from a one-roll to a two-roll pattern. A closer inspection of both plots suggests, however, that an increase of the portion of the total heat transfer due to the primary mode causes a decrease of that of the secondary mode. This is clearly indicated for $\Gamma = 0.5$ and 1 in both $Ra = 10^7$ and 10^8 series, and for $\Gamma = 2$, 2.5 and 3 in the series with $Ra = 10^8$. It further supports our arguments in the last paragraph. The local minimum of the secondary POD mode contribution coincides with the local maximum of the primary one. When the primary mode becomes less efficient in transferring heat, the secondary mode has to take a bigger share. The two panels in figure 11 display finally the time dependence of the expansion coefficients of the first three POD modes, $a_m(t)$ with $m = 1, 2, 3$. The graphs are obtained by projecting the 100 snapshots onto the POD modes $\phi_i^{(m)}(\boldsymbol{x})$ for $m = 1, 2, 3$. While the primary modes remains nearly constant, we see that the secondary and tertiary modes oscillate with a period of approximately $30t_f$ and are shifted with respect to each other by about $10t_f$. The secondary and tertiary mode contribute thus mainly to temporal variance of the heat transfer. Their time-averaged contributions remain, however, significantly lower than that of the primary mode.

6. Summary and discussion

Within the parameter range of the present study, the DNS results have revealed a dependence of the Nusselt number on the aspect ratio. The variation in $Nu(\Gamma)$ curve is between 11 % and 3%, depending on the Rayleigh number and the range of accessible aspect ratios. A minimum of $Nu(\Gamma)$ is found at $\Gamma \approx 2.5$ and $\Gamma \approx 2.25$ for $Ra = 10^7$ and $Ra = 10^8$, respectively. This is exactly the point where the LSC undergoes a transition from a single-roll to a double-roll pattern. The trend in $Nu(\Gamma)$ curve indicates that the heat transfer becomes independent of the aspect ratio of the cylindrical cell for sufficiently large aspect ratios. This is $\Gamma \gtrsim 8$ at $Ra = 10^7$ and $\Gamma > 8$ for $Ra \geqslant 10^8$. The LSC patterns reorganize from roll shape to pentagonal or hexagonal structures with increasing Γ and fixed Ra as well as with increasing Ra and fixed Γ.

We provide arguments, which rationalize the non-monotonic graphs $Nu = f(\Gamma)$. Furthermore, we demonstrate that the power law relation $Nu = A \times Ra^{\beta}$ gives rise to a coefficient $A(\Gamma)$ which decreases from 0.165 to 0.118 and an exponent $\beta(\Gamma)$ which increases from 0.287 to 0.305. Furthermore, they follow algebraic scaling relations $A(\Gamma) \sim \Gamma^{-\lambda_1}$ and $\beta(\Gamma) \sim \Gamma^{\lambda_2}$, with $\lambda_1 = 0.18$ and $\lambda_2 = 0.03$ for aspect ratios between 0.5 and 4 and Rayleigh numbers between 10^7 and 10^9. We believe that it is important to include this dependence, albeit weak, in future scaling theories. The variation of β seems to bridge the gap between the well-known exponents $\beta = 2/7$ and $1/3$, which have been measured in the past. Further studies at higher Rayleigh numbers and larger aspect ratios have to be conducted to draw a firm conclusion on the robustness of the observed scaling. We cannot comment on the trend with respect to Prandtl number, which will exist as indicated in Hartlep *et al.* (2005).

The primary POD mode contains most of the energy, and transports about one-half of the global heat for $\Gamma \geqslant 1$. Their contribution to the total heat transfer varies with Γ and Ra as indicated in table 3. This has been demonstrated with the help of a Karhunen–Loève analysis of samples of turbulent convection field. We also observe that the LSC patterns in turbulent convection at $Ra \geqslant 10^7$ are still strikingly similar to those in the weakly nonlinear regime immediately beyond the onset of convection (Bodenschatz *et al.* 2000). The system does not seem to 'forget' these patterns. This might partly be attributed to the closed volume, in which the studies are conducted. An LSC is, therefore, always present similar to high-Reynolds number turbulence in von Kármán swirling flows (La Porta *et al.* 2001) or Taylor vortex flows (Lathrop *et al.* 1992).

One possible argument against our observation of Γ-dependent Nusselt number could be that the Rayleigh number for the given Prandtl number $Pr = 0.7$ is still too small and that the convective turbulence has not yet reached the so-called hard turbulence regime, as discussed for example by Castaing *et al.* (1989). In order to weaken this argument, we determine the dissipation scale and relate it to the height of the cell. Since $Pr < 1$, the diffusive scale of the temperature, the Corrsin scale $\eta_c = (\kappa^3/\langle\epsilon\rangle)^{1/4}$, is larger than the Kolmogorov scale $\eta_K = (\nu^3/\langle\epsilon\rangle)^{1/4}$. The scale separation ratio gives: $H/\eta_K = 133$, 278 and 588 for $Ra = 10^7$, 10^8 and $Ra = 10^9$, respectively. Here η_K is directly evaluated from the energy dissipation field as discussed in § 2. Even if we take a fraction of H, the scale separation is of $O(10^2)$. Furthermore, for all the Rayleigh numbers discussed here, we reported strongly non-Gaussian temperature statistics in Emran & Schumacher (2008), which clearly indicate that the convective motion is in a state of fully developed turbulence.

Further numerical simulations and experiments in the regime of large aspect ratio and high Rayleigh number are necessary. One can expect that the aspect ratio

dependence of the turbulent heat transfer will disappear for sufficiently large Γ and that turbulent convection approaches an asymptotic geometric regime in which the physics becomes independent of sidewall effects. To achieve those goals, some efforts are underway for the cylindrical case and will hopefully shed more light on the dependencies $A(\Gamma)$ and $\beta(\Gamma)$ in the heat transport law as reported in figure 4. Another important aspect, in our view, would be to conduct a closer study of the same issues for fixed flux boundary conditions (which correspond, for example, to a radiative cooling on top of an atmospheric boundary layer). Recently, the first step in this direction has been undertaken by Verzicco & Sreenivasan (2007) and Johnston & Doering (2008).

We wish to thank Roberto Verzicco for providing us his simulation code and his help at the beginning of our studies. The authors also acknowledge the support by the Deutsche Forschungsgemeinschaft (DFG) under grant SCHU1410/2-1 and by the Heisenberg Program of the DFG under grant SCHU 1410/5-1. The largest DNSs have been carried at the Jülich Supercomputing Centre (Germany) under grants HMR09 and HIL03. We thank F. H. Busse, C. R. Doering, S. Grossmann, K. R. Sreenivasan, A. Thess and K.-Q. Xia for helpful comments and suggestions. The work is also benefitted from the constructive comments by the three anonymous referees.

REFERENCES

Ahlers, G., Grossmann, S. & Lohse, D. 2009 Heat transfer and large-scale dynamics in turbulent Rayleigh–Bénard convection. *Rev. Mod. Phys.* **81**, 503–537 .

Amati, G., Koal, K., Massaioli, F., Sreenivasan, K. R. & Verzicco, R. 2005 Turbulent thermal convection at high Rayleigh numbers for Boussinesq fluid of constant Prandtl number. *Phys. Fluids* **17**, 121701.

Bodenschatz, E., Pesch, W. & Ahlers, G. 2000 Recent developments in Rayleigh–Bénard convection. *Annu. Rev. Fluid Mech.* **32**, 709–778.

Brown, E. & Ahlers, G. 2008 Azimuthal asymmetries of the large-scale circulation in turbulent Rayleigh–Bénard convection. *Phys. Fluids* **20**, 105105.

Bukai, M., Eidelman, A., Elperin, T., Kleeorin, N., Rogachevskii, I. & Sapir-Katiraie, I. 2009 Effect of large-scale coherent structures on turbulent convection. *Phys. Rev.* E **79**, 066302.

Busse, F. H. 2003 The sequence-of-bifurcations approach towards understanding turbulent fluid flow. *Surv. Geophys.* **24**, 269–288.

Busse, F. H. & Whitehead, J. A. 1971 Instabilities of convection rolls in a high Prandtl number fluid. *J. Fluid Mech.* **47**, 305–320.

Castaing, B., Gunaratne, G., Heslot, F., Kadanoff, L., Libchaber, A., Thomae, S., Wu, X.-Z., Zaleski, S. & Zanetti, G. 1989 Scaling of hard thermal turbulence in Rayleigh–Bénard convection. *J. Fluid Mech.* **204**, 1–30.

Charlson, G. S. & Sani, R. L. 1970 Thermoconvective instability in a bounded cylindrical fluid layer. *Intl J. Heat Mass Transfer* **13**, 1479–1496.

Charlson, G. S. & Sani, R. L. 1971 On the thermoconvective instability in a bounded cylindrical fluid layer. *Intl J. Heat Mass Transfer* **14**, 2157–2160.

Ching, E. S. C. & Tam, W. S. 2006 Aspect-ratio dependence of heat transport by turbulent Rayleigh–Bénard convection. *J. Turbul.* **7**, N 72.

Clever, R. M. & Busse, F. H. 1989 Three-dimensional knot convection in a layer heated from below. *J. Fluid Mech.* **198**, 345–363.

Croquette, V. 1989 Convective pattern dynamics at low Prandtl number. Part II. *Contemp. Phys.* **30**, 153–171.

Emran, M. S. & Schumacher, J. 2008 Fine-scale statistics of temperature and its derivatives in convective turbulence. *J. Fluid Mech.* **611**, 13–34.

Fitzjarrald, D. E. 1976 An experimental study of turbulent convection in air. *J. Fluid Mech.* **73**, 693–719.

Funfschilling, D., Brown, E., Nikolaenko, A. & Ahlers, G. 2005 Heat transport by turbulent Rayleigh–Bénard convection in cylindrical samples with aspect ratio one and larger. *J. Fluid Mech.* **536**, 145–154.

Gao, H., Metcalfe, G., Jung, T. & Behringer, R. P. 1987 Heat-flow experiments in liquid ^{4}He with variable cylindrical geometry. *J. Fluid Mech.* **174**, 209–231.

Grossmann, S. & Lohse, D. 2000 Scaling in thermal convection: a unifying theory. *J. Fluid Mech.* **407**, 27–56.

Grossmann, S. & Lohse, D. 2003 On geometry effects in Rayleigh–Bénard convection. *J. Fluid Mech.* **486**, 105–114.

Grötzbach, G. 1983 Spatial resolution requirements for direct numerical simulation of the Rayleigh–Bénard convection. *J. Comput. Phys.* **49**, 241–269.

von Hardenberg, J., Parodi, A., Passoni, G., Provenzale, A. & Spiegel, E. A. 2008 Large-scale patterns in Rayleigh–Bénard convection. *Phys. Lett.* A **372**, 2223–2229.

Hartlep, T., Tilgner, A. & Busse, F. H. 2003 Large scale stuctures in Rayleigh–Bénard convection at high Rayleigh numbers. *Phys. Rev. Lett.* **91**, 064501.

Hartlep, T., Tilgner, A. & Busse, F. H. 2005 Transition to turbulent convection in a fluid layer heated from below at moderate aspect ratio. *J. Fluid Mech.* **544**, 309–322.

Johnston, H. & Doering, C. R. 2009 A comparison of turbulent thermal convection between conditions of constant temperature and constant flux. *Phys. Rev. Lett.* **102**, 064501.

Kerr, R. M. 1996 Rayleigh number scaling in numerical convection. *J. Fluid Mech.* **310**, 139–179.

Koschmieder, E. 1969 On the wavelength of convective motions. *J. Fluid Mech.* **35**, 527–530.

La Porta, A., Voth, G. A., Crawford, A. M., Alexander, J. & Bodenschatz, E. 2001 Fluid particle accelerations in fully developed turbulence. *Nature* **409**, 1017–1019.

Lathrop, D. P., Fineberg, J. & Swinney, H. L. 1992 Turbulent flow between concentric rotating cylinders at large Reynolds numbers. *Phys. Rev. Lett.* **68**, 1515–1518.

Niemela, J. J., Skrbek, L., Sreenivasan, K. R. & Donelly, R. J. 2000 Turbulent convection at very high Rayleigh numbers. *Nature* **404**, 837–840.

Niemela, J. J. & Sreenivasan, K. R. 2006 Turbulent convection at high Rayleigh numbers and aspect ratio 4. *J. Fluid Mech.* **557**, 411–422.

Oresta, P., Stringano, G. & Verzicco, R. 2007 Transitional regimes and rotation effects in Rayleigh–Bénard convection in a slender cylindrical cell. *Eur. J. Mech.* B/*Fluids* **26**, 1–14.

Pope, S. B. 2000 *Turbulent Flows*. Cambridge University Press.

du Puits, R., Resagk, C. & Thess, A. 2007 Breakdown of wind in turbulent thermal convection. *Phys. Rev.* E **75**, 016302.

van Reeuwijk, M., Jonker, H. J. J. & Hanjalić, K. 2008 Wind and boundary layers in Rayleigh–Bénard convection. I. Analysis and modelling. *Phys. Rev.* E **77**, 036311.

Shishkina, O. & Wagner, C. 2006 Analysis of thermal dissipation rates in turbulent Rayleigh–Bénard convection. *J. Fluid Mech.* **546**, 51–60.

Shishkina, O. & Wagner, C. 2008 Analysis of sheet-like thermal plumes in turbulent Rayleigh–Bénard convection. *J. Fluid Mech.* **599**, 383–404.

Siggia, E. D. 1994 High Rayleigh number convection. *Annu. Rev. Fluid Mech.* **26**, 137–168.

Sirovich, L. & Park, H. 1990 Turbulent thermal convection in a finite domain. Part I. Theory. *Phys. Fluids* A **2**, 1649–1668.

Smith, T. R., Moehlis, J. & Holmes, P. 2005 Low-dimensional modelling of turbulence using Proper Orthogonal Decomposition: a tutorial. *Nonlinear Dyn.* **41**, 275–307.

Stein, R. F. & Nordlund, A 2006 Solar small-scale magnetoconvection. *Astrophys. J.* **642**, 1246–1255.

Sun, C., Ren, L.-Y., Song, H. & Xia, K.-Q. 2005 Heat transport by turbulent Rayleigh–Bénard convection in 1 m diameter cylindrical cells of widely varying aspect ratio. *J. Fluid Mech.* **542**, 165–174.

Strogatz, S. H. 1994 *Nonlinear Dynamics and Chaos*. Westview Press.

Verzicco, R. & Camussi, R. 2003 Numerical experiments on strongly turbulent thermal convection in a slender cylindrical cell. *J. Fluid Mech.* **477**, 19–49.

Verzicco, R. & Orlandi, P. 1996 A finite-difference scheme for three-dimensional incompressible flows in cylindrical coordinates. *J. Comput. Phys.* **123**, 402–414.

Verzicco, R. & Sreenivasan, K. R. 2007 A comparison of turbulent thermal convection between conditions of constant temperature and constant heat flux. *J. Fluid Mech.* **595**, 203–219.

Wu, X.-Z. & Libchaber, A. 1992 Scaling relation in thermal turbulence: the aspect-ratio dependence . *Phys. Rev.* A **45**, 842–845.

Zerihun Desta, T., Van Brecht, A., Quanten, S., Van Buggenhout, S., Meyers, J., Baelmans, M. & Berckmans, D. 2005 Modelling and control of heat transfer phenomena inside a ventilated air space. *Energy Build.* **37**, 777–786.

Xi, H.-D. & Xia, K.-Q. 2008*a* Azimuthal motion, reorientation, cessation and reversal of the large-scale circulation in turbulent thermal convection: a comparative study in aspect ratio one and one-half geometries. *Phys. Rev.* E **78**, 036326.

Xi, H.-D. & Xia, K.-Q. 2008*b* Flow mode transitions in turbulent thermal convection. *Phys. Fluids* **20**, 055104.

Zhou, Q., Sun, C. & Xia, K.-Q. 2007 Morphological evolution of thermal plumes in turbulent Rayleigh–Bénard convection. *Phys. Rev. Lett.* **98**, 074501.